Bulletin of the Mineral Research and Exploration

http://bulletin.mta.gov.tr

Investigation of gas and gas hydrate accumulations along the continental margin of the Danube Delta (Romania and Bulgaria offshore) using seismic reflection data

Orhan ATGIN[a*] and Günay ÇİFCİ[a,b]

[a] *Dokuz Eylül University, Institute of Marine Sciences and Technology, İzmir, Türkiye*
[b] *Dokuz Eylül University, Department of Geophysics, İzmir, Türkiye*

Research Article

Keywords:
Danube Channel-Levee System, Multiple BSR, MTD, Geothermal Gradient.

ABSTRACT

In 2012, a comprehensive study of the Danube River's submarine channels continental slope was conducted, employing multi-beam bathymetry and over 2300 km of high-resolution two-dimensional seismic reflection data. The investigation aimed to delve into the area's morphology, potential for gas hydrate presence, and the correlation between stratigraphic units and gas hydrates. Three distinct zones, revealed Bottom Simulating Reflectors (BSRs) indicating the base of gas hydrate accumulations in the seismic data. These BSR areas exhibited Type-1 reflections, characterized by continuous cuts across layers. Notably, five discrete levels of BSRs were detected, suggesting a consistent gas composition across them. The multiple BSR formations are attributed to higher sedimentation rates relative to gas hydrate dissolution rates. Mass transport deposits (MTDs) within the gas hydrate stability zone (6 in total) were identified; their highly consolidated nature could account for the absence of gas hydrates within them. Additionally, one MTD displayed elevated heat flow measurements, indicating a higher geothermal gradient, likely due to its relatively high thermal conductivity. This disparity in thermal properties explains the deeper-than-expected BSR in this specific region, as it forms at a lower temperature equilibrium level due to efficient heat conduction.

Received Date: 01.11.2023
Accepted Date: 28.12.2023

1. Introduction

Gas hydrates are crystalline compounds consisting of gas molecules trapped within water molecules, forming under high pressure and low-temperature conditions. The parameters that control the formation and stability of gas hydrates are the hydrate's structure, pressure, temperature, gas components, and ionic forces (Sloan and Koh, 2007; Thakur and Rajput, 2010). They are commonly found in permafrost regions and oceanic sediments along continental margins. For the formation of gas hydrates, it is necessary to have a high production of methane gas in the environment and ensure suitable thermobaric conditions. The stability of gas hydrates is governed by pressure changes; a decrease in pressure or an increase in temperature leads to the dissociation of the hydrate structure into water and methane gas (Lerche and Bagirov, 1998). The maximum depth at which a gas hydrate layer can form is associated with the geothermal gradient and is limited by increasing temperatures (Kvenvolden, 1995). Hence, gas hydrates can be observed at depths where they can remain under the equilibrium conditions of temperature and pressure for hydrate stability.

Interest in gas hydrates primarily arises from three reasons: 1) The environmental consequences

Citation Info: Atgın, O., Çifci, G. 2024. Investigation of gas and gas hydrate accumulations along the continental margin of the Danube Delta (Romania and Bulgaria offshore) using seismic reflection data. Bulletin of the Mineral Research and Exploration 175, 19-40. https://doi.org/10.19111/bulletinofmre.1411403

**Corresponding author: Orhan ATGIN, orhan.atgin@deu.edu.tr*

of methane release from gas hydrates on the seafloor, which contributes to the greenhouse effect when released into the atmosphere. 2) The geohazards that gas hydrates to pose dissociation could due to their potential impact on seafloor stability. 3) The potential of gas hydrates as an energy source because they contain a significant amount of methane (Holbrook, 1996; Çifci, 2020). Under standard temperature and pressure conditions, 1 m^3 of gas hydrate contains 163 m^3 of free gas (Lee et al., 2011).

Gas hydrates create distinctive reflections known as Bottom Simulating Reflectors (BSR) in seismic sections, making them identifiable and mappable. BSRs are prominent reflections caused by the negative impedance contrast between sediment layers containing high-velocity gas hydrates above and low-velocity gas-bearing sediments below (Hyndman and Davis, 1992). BSRs are reflections that adhere to isothermal surfaces, mimicking the topography of the ocean floor. Their formation disregards the dip of stratigraphic units, allowing them to traverse stratigraphic layers.

BSRs have reverse polarity compared to the seafloor in seismic sections, and their amplitudes are generally higher than those of surrounding reflections. Even minimal concentrations of free gas, typically just a few percent in the pore volume beneath the gas hydrate region, are sufficient for the formation of BSRs (Andreassen et al., 2007; Haacke et al., 2007).

Numerous gas hydrate research studies worldwide have observed BSR. Some of these well-studied areas include the Nankai Trough in Japan (Ashi et al., 2002; Baba and Yamada, 2004), the Hydrate Ridge off the eastern coast of the United States (Tréhu et al., 2004; Bangs et al., 2011), the Ulleung Basin off the east coast of Korea (Horozal et al., 2009; Riedel et al., 2012; Yoo et al., 2013), and the Gulf of Mexico (Milkov and Sassen, 2000; Cook et al., 2014). In addition to these studies, many gas hydrate investigations, particularly along continental margins, have been conducted worldwide and continue to be ongoing.

In the Black Sea, where the study area is located, several studies have established the presence of gas hydrates. Samples taken from some mud volcanoes in the deep basin and southern Crimea have confirmed the presence of gas hydrates (Ivanov et al., 1996; Woodside et al., 1997). Pape et al. (2011) analyzed gas hydrate samples from BSR-observed regions off the coast of Hopa in the Black Sea. Extensive gas hydrate reservoirs between Sakarya and Cide on the Turkish western margin of the Black Sea have been identified through seismic studies (Dondurur, 2021). In the eastern margin of the Black Sea, BSR reflections have been interpreted in the multi-channel seismic reflection data from ridge structures off Trabzon (Minshull et al., 2020).

Multiple stacked BSRs can occasionally observed. These rare occurrences of multiple BSRs have been documented in various regions, including the Norwegian margin (Posewang and Mienert, 1999; Andreassen et al., 2000), the Nankai Trough (Foucher et al., 2002; Baba and Yamada, 2004), the gas hydrate ridge off the Cascadia continental margin (Tréhu et al., 2004; Bangs, 2005), on the western margin of Türkiye, off Zonguldak and Amasra (Küçük, 2016) and one of the most striking examples globally, the Danube Fan Delta, which includes the study area (Popescu et al., 2006).

In the case of multiple BSRs, the uppermost BSR is typically interpreted to represent the base of the gas hydrate stability zone (BGHSZ), while the origin of the deeper BSRs continues to be a subject of debate. The presence of multiple BSRs in seismic sections was first demonstrated by Popescu et al. (2006). The SUGAR (Submarine Gas Hydrate Reservoirs) project, led by the German GEOMAR institute in 2013 and that provides some of the data used in this study, is one of the significant projects in this area. With the goal of developing a method for natural gas production from gas hydrates using CO_2 injection, the project generated data that contributed to various studies related to gas hydrate research, including those by Zander et al. (2017), Hillman et al. (2018), and Pape et al. (2020).

This study utilizes high-resolution two-dimensional multichannel seismic reflection data to investigate the characteristics and distribution of BSRs in the channel-levee system that makes up the Danube deep-sea fan. The research focuses on the

characteristic features of the multiple BSRs in the study area, their relationships with seismic facies and Mass Transport Deposit (MTD) structures, and the mechanisms governing the formation of these multiple BSRs.

1.1. Regional Geology

The Black Sea, with its deepest point at 2200 meters, is an inland sea connected to the Mediterranean via the Dardanelles and Bosporus Straits. It is one of the world's largest intercontinental basins (Figure 1).

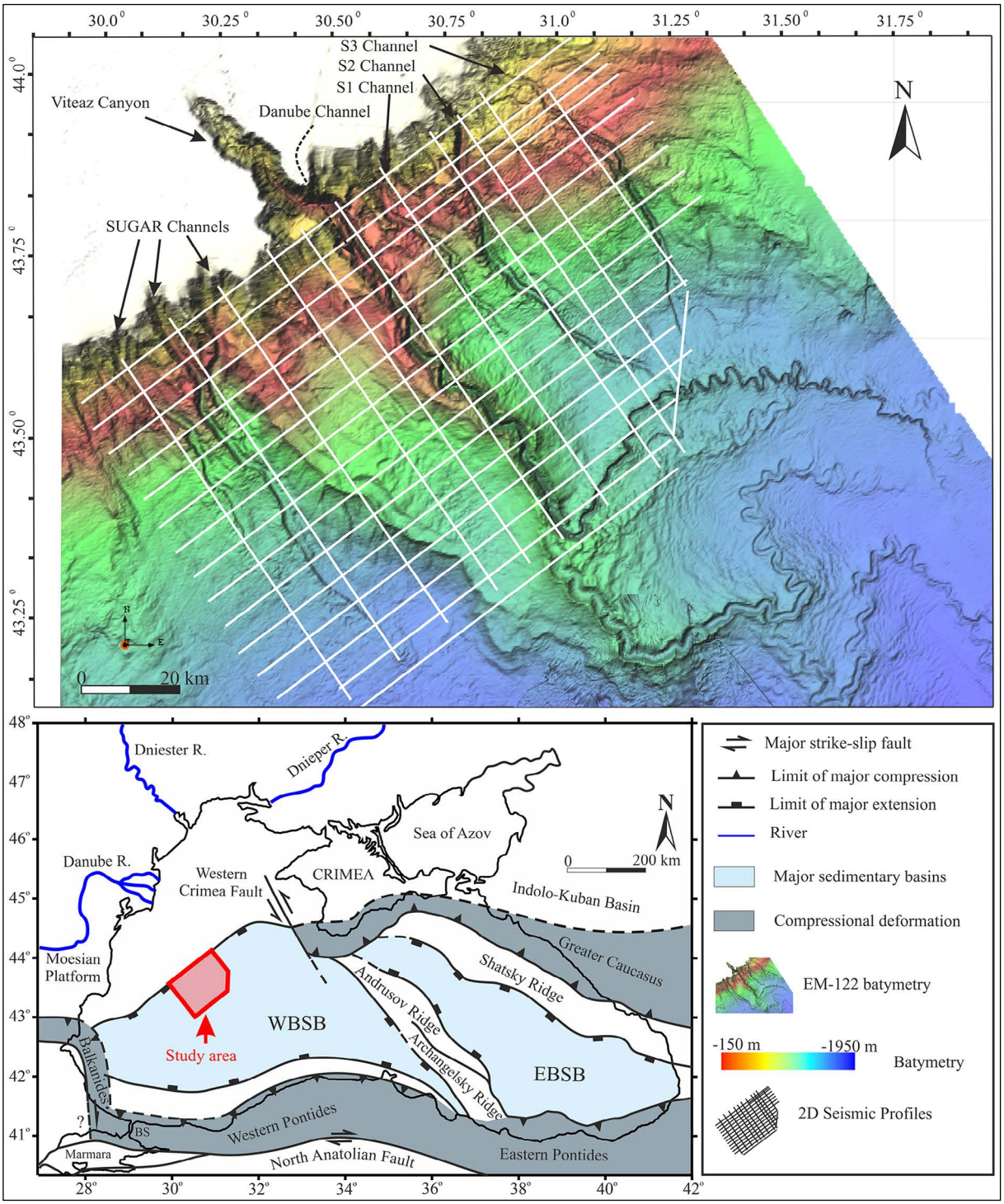

Figure 1- Main tectonic elements of the Black Sea and its surroundings and the view of seismic faults on the bathymetry (Modified from Robinson et al., 1996; Finetti et al., 1988; Kazmin et al., 2000). WBSB, Western Black Sea Basin; EBSB, Eastern Black Sea Basin.

Although the formation of the Black Sea is associated with rifting tectonics, this process concluded during the Eocene epoch, and the boundaries of the Black Sea are now predominantly characterized by compressional deformation (Robinson et al., 1996).

While the Black Sea is currently considered a single basin in terms of bathymetry, seismic data reveal that this basin comprises two distinct sub-basins known as the Eastern Black Sea Basin (EBSB) and the Western Black Sea Basin (WBSB; Tugolesov et al., 1985; Finetti et al., 1988; Belousov and Volvovsky, 1989; Starostenko et al., 2004). These basins are separated by the Andrusov and Arkhangelsky Ridges (Figure 1). The largest continental shelf area in the Black Sea Basin is the Odessa Shelf located in the western part (Nikishin et al., 2015).

The study area is located in the northwestern margin of the Black Sea, where the Danube River flows into the sea (Figure 1). The deep-sea fans of the Danube and Dnieper rivers are believed to have begun developing approximately 900 ka ago (Winguth et al., 2000). These fans were formed as a result of the sedimentary deposits of the Danube, Dnieper, Dniester, and Bug rivers during the last glacial period (Winguth et al., 2000; Popescu et al., 2001). The Danube Fan is a fine-grained turbidite system separated from the coastal shelf by an extensive shelf break (approximately 120 km) (Popescu et al., 2001). The Danube deep-sea fan developed in a sloping region, ranging from 100 m water depth at the shelf break to 2200 m water depth on the abyssal plain (Wong et al., 1997). The most recent active channel of the Danube fan is the Danube Channel, which connects to the Danube River in the Viteaz Canyon at the shelf break (Figure 1) (Popescu et al., 2001). The erosive Viteaz Canyon terminates in a channel-levee system at approximately 800 m water depth (Lericolais et al., 2013). The Danube Channel formed approximately 25 ka/years/million years ago during a period when sea levels were about 120 m lower than today (Winguth et al., 2000).

The formation of gas hydrates in the Danube fan has been known since the first hydrate discoveries in shallow submarine sediments (Yefremova and Zhizhchenko, 1974; Ginsburg, 1998). More recently, the presence of gas hydrates in deep sediments has been inferred from BSR observations in the southern part of the fan (du Fornel, 1999). Gas emissions in the region consist primarily of biogenic methane, with concentrations ranging from 99.1% to 99.9% (Poort et al., 2005; Römer et al., 2012; Bialas et al., 2014).

1.2. Data and Method

As part of the collaborative efforts of the SUGAR project conducted by GEOMAR, seismic equipment belonging to Dokuz Eylül University's Institute of Marine Sciences and Technology, in conjunction with the R/V Maria S. Merian research vessel, collected approximately 2300 km of high-resolution multichannel seismic reflection data in December 2013. The seismic survey lines are shown in Figure 1. A seismic receiver cable, 1050 m in length, with 196 channels at 6.25-m group intervals, was towed from a depth of 4 m. Seismic shots were generated using a GI-gun source, which was towed from a depth of 3 m and had a volume of 45+105 inch^3. Shots were fired at intervals of 12.5 m and 18.75 m. The seismic recordings had a sampling interval of 1 ms and a total record length of 5000 ms.

The multichannel seismic data underwent several traditional data processing steps in sequence, including data loading, geometry definition, bandpass filtering (8-220 Hz), trace editing, f-k slope filtering, suppression of multiples (SRME - Surface-Related Multiple Elimination), CDP group formation, velocity analysis, pre-stack time migration, and amplitude corrections. For stratigraphic interpretations, automatic gain control (AGC) was used, while for BSR interpretations, true amplitude recovery (TAR) was applied to the data. Seismic sections with balance curves calculated on top of the BSR levels were subjected to pre-stack depth migration. Envelope sections were obtained from the final sections for complex seismic attribute analysis.

The EM122 multibeam bathymetry system, mounted on the ship's hull, collected data simultaneously with all seismic lines. From this data, a bathymetry map with a resolution of 25m x 25m was obtained. The EM122 system is a multibeam

bathymetry system from Kongsberg that operates at a frequency of 12 kHz and collects 432 beams of data.

In the areas where BSRs were observed, a heat flow probe was used to obtain information about in-situ sediment temperature and thermal conductivity. The probe has an active length of 5.67 meters and is equipped with 22 evenly spaced temperature sensors. Each sensor measures temperature with a resolution of less than 1 mK, and these sensors are calibrated with an accuracy of better than 2 mK.

2. Main Text

Within the stratigraphic levels formed by the Danube channel-levee systems, BSRs have been observed in three different areas, with some of these areas exhibiting multiple BSR reflections. The acoustic data penetrate the entire Plio-Quaternary-aged units, which contain numerous geological features. The area contains multiple paleo-channel-levee systems and mass transport deposits (MTD) from past periods. Additionally, in some parts of the study area, acoustic masking (acoustic turbidites) sometime disrupts the structure of seismic signals and hinder the observation of the continuity of layers the following sub-sections. In this section, all of these elements have been individually addressed.

2.1. Morphological Features of Study Area

In the Romanian economic zone, the continental shelf, which has a width of approximately 160 km and a slope of 10°. It is breached by the Viteaz Canyon, which has a width of 6 km, a length of 30 km, and a depth of 900 m. The shelf break in this region is located at approximately 120 m in depth. Compared to other slopes in the Black Sea, the continental slope in this area is quite long with an approximate 5-degree slope. The slope between approximately 200 and 500 m contours is steeper in this region compared to the rest of the margin, with a slope of 10°. The most significant structural and morphological feature in the study area is the Viteaz Canyon, which extends to the shelf break and connects to the Danube Channel. The Danube Channel, which has a wide thalweg on the continental slope and progresses relatively linearly, transforms into a narrow channel with an increasing sinuosity as it approaches the abyssal plain. In addition to the Danube Channel, there are several other channel systems in the study area. None of these channels, including three located to the west and three to the east of the Danube Channel, are on the same scale as the Danube Channel itself. To the west of the Danube Channel, three adjacent channels begin with a canyon system from the shelf break and end within the continental slope. These channels have been referred to as the "SUGAR Channels" in Zander et al. (2017). To the east of the Danube Channel, there are three channel systems that start with a canyon system from the shelf break and terminate within the continental slope. These have been labeled as "S1, S2, and S3" in Hillman et al. (2018) (Figure 1).

In the seismic profiles from Nikishin et al. (2015) covering the entire Black Sea, the maximum depth of the fan systems in the region with Danube submarine fans is approximately 4 seconds in two-way travel time. The choice of a 5-second two-way travel time as the recording length of the seismic reflection sections in the study enabled the observation of all units created by the channel-levee systems. These units are influenced by the geometry and levees created by both the current Danube Channel and the geometries and levees of paleo-channels. Both the geometry and levees created by the current channel and the geometries and levees of the paleo-channels have developed downslope in a southwest-northeast direction.

2.2. Distribution and Characteristics of BSRs

The BSRs are observed starting at a depth of 665 m and ending at the deepest point of the study area, which is 1890 m (Figure 2). The depth information for these BSR regions is provided in Table 1. Hyndman and Davis (1992) identified the Type-1 BSR reflections, known as BSRs, which intersect the layers and appear as continuous reflections throughout the study area. All BSRs in the study area, whether in multiple or single reflection forms, are of Type-1 category, and acoustic turbidity zones induced by free gas have not formed beneath them. Furthermore, all Type-1 BSR exhibit a reverse-polarity reflection character compared to the seafloor (Figure 3).

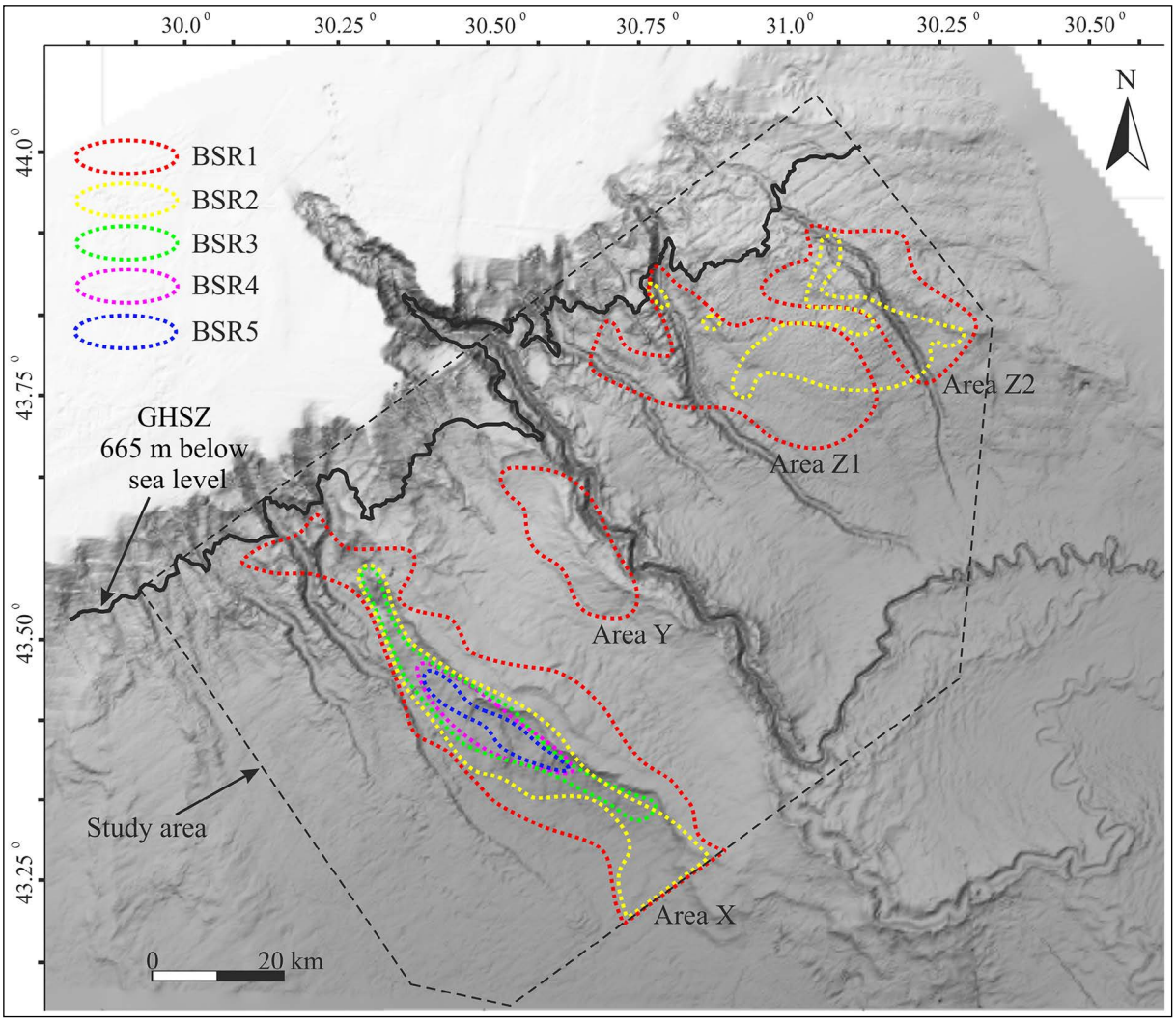

Figure 2- Distribution map of BSRs in the study area. BSRs in the area are grouped into three separate areas referred to as "X," "Y," and "Z."

BSRs are observed in three distinct regions, labeled as "X, Y, and Z" (Figure 2). In the westernmost region X the uppermost and most extensive BSR, which spreads over the largest area 825 km^2, referred to as "BSR1". The "X" BSR area extends from the shallowest region, 665 m to the deepest part of the area, 1890 m. Subsequently, the "Z" area, covering 714 km^2, follows, and the "Y" area, covering 172 km^2, is the smallest in terms of surface area among the BSR areas (Table 1). The prominent "X" area, comprises multiple BSRs consisting of 5 layers (Figures 3a, b). The multiple BSRs are numbered from shallow to deep in the acoustic data, with the reflection furthest down being "BSR5." The 5-layered BSRs in the "X" area gradually decrease in surface area with depth (Figure 2).

The "Y" area is the smallest BSR area in terms of surface area. Throughout this entire area, only the "BSR1" reflection was observed (Figures 3c and d).

In the "Z" area, only "BSR1 and BSR2" were observed. While the distribution of the other two areas is oriented northwest to southeast along the slope, the "Z" area exhibits a more irregular geometry compared to the others. Mass transport deposit (MTD) divides the "Z" area in a southwest-northeast direction, and the area is divided into two parts (Figures 2e, 2f, and 5b). Area to the west is referred to as "Z1," and the area to the east is referred to as "Z2." Although the multiple BSRs within the "X" area are distributed in a consistend manner "BSR1 and BSR2" display somewhat unrelated geometries, within the "Z" area (Figure 2). The surface area and depth relative to the

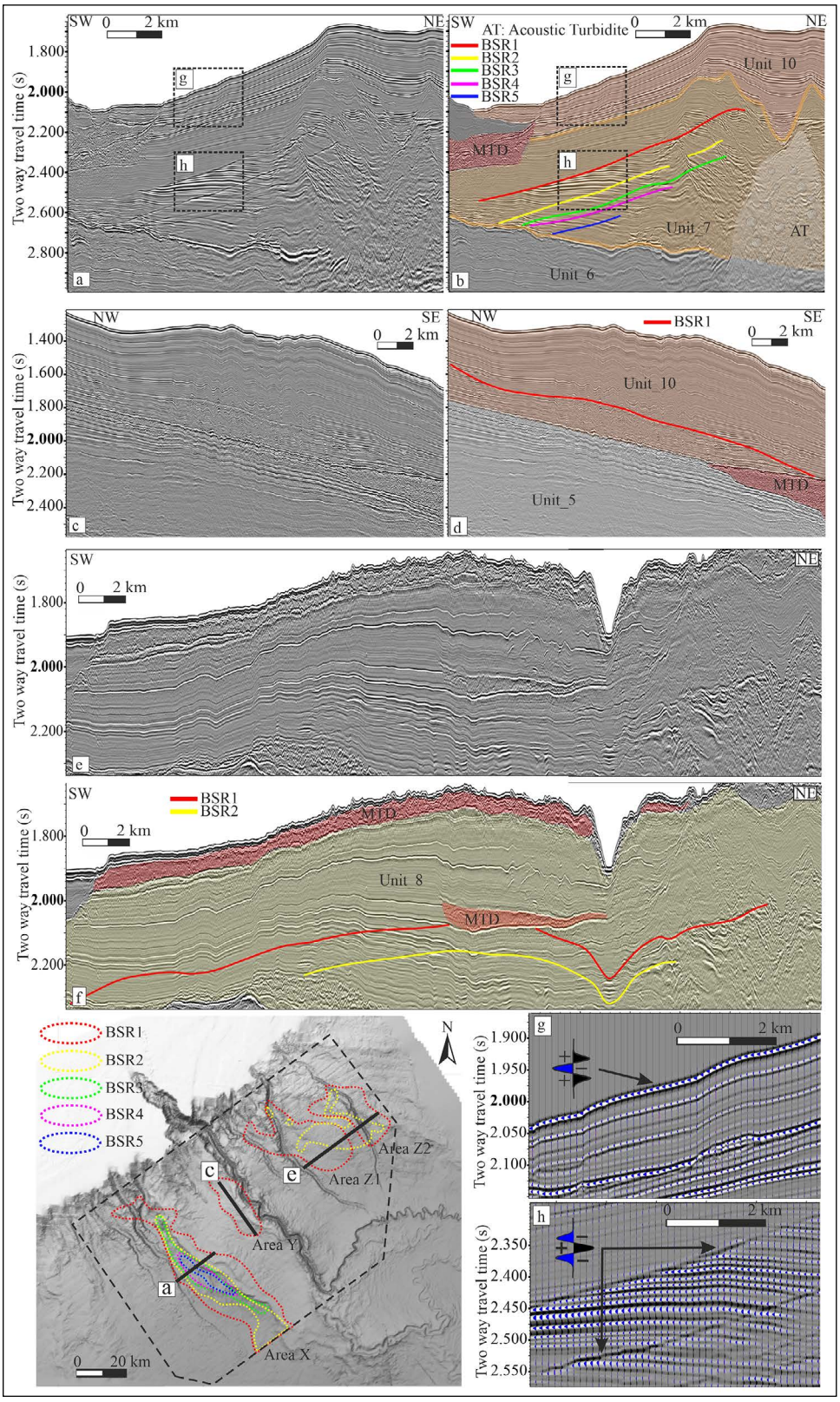

Figure 3- Samples of BSRs from seismic sections in the study area, a) Sample seismic section from the "X" BSR area and b) its interpreted version, c) sample seismic section from the "Y" BSR area and d) its interpreted version, e) sample seismic section from the "Z" BSR area and f) its interpreted version. g) Seafloor reflection in the "X" BSR area and h) the polarities of BSR1 and BSR2 in the same area. The polarities of BSRs are inverted compared to the seafloor reflection. MTD indicates mass transport deposits.

seafloor for all primary and multiple BSRs are shown in Table 1.

Table 1- Surface areas (km^2) and depth ranges (m) of all BSRs in the study area.

Area	Surface Area (km^2)	Depth Range (m)
X_BSR1	825	665-1890
X_BSR2	359	1150-1890
X_BSR3	180	1150-1807
X_BSR4	111	1370-1700
X_BSR5	60	1310-1680
Y_BSR1	172	856-1275
Z1_BSR1	444	665-1518
Z1_BSR2	105	665-1285
Z2_BSR1	266	840-1580
Z2_BSR2	88	886-1340

The presence of multiple BSRs has been observed for more than 10 years using three different seismic recording systems, as defined by Popescu et al. (2006). These observations indicate that the five BSR reflections in the region are not artificial reflections, errors, or unreal images caused by recording system problems. The BSRs observed in this study are consistent with the multiple BSRs observed in previous studies in the region.

2.3. Seismic Facies Associated with BSR

Sediments transported by the Danube River are carried to deep-sea via the Viteaz Canyon. In Figure 4, on the seismic line that intersects the Danube Channel, it is possible to see all the geological features created by the channel-levee systems. These units are numbered from 1 to 11 with the unit formed by the recent Present-day Danube Channel being represented by number 10. Chaotic reflections in the acoustic data known as Mass Transport Deposits (MTDs) where regular reflections are absent (Figures 3b, d, e, and Figure 4). Winguth et al. (2000) have defined the ages of these channel-levee systems. The age of the Present Danube Channel-Levee System (DCS) corresponds to the last major glacial period and is estimated to be 0-75 ka years old. Unit number 9, which is located above the buried channel-levee system (BCS) and to the west of the paleo-channel, is estimated to be 75-320 ka years old, while the unit corresponding to the BCS buried to the west and below the Danube Channel is estimated to be 320-500 ka years old (Figure 4) (Winguth et al., 2000).

The seismic line in Figure intersects all 3 areas where BSRs are observed. All the BSRs in the westernmost “X” area are located within unit number 7, which is the buried channel-levee system (BCS). For this region, neither primary nor multiple BSRs have been observed in any unit other than BCS. Except for the top BSR1 reflection, all other BSRs have terminated at the boundary where acoustic turbidites are found to the east and the intersection of units 6 and 7 to the west. In the “Y” area, where only “BSR1” is observed, this reflection is entirely contained within unit number 10, which is the Danube Channel-Levee System (DCS). The BSR1 in this area is bounded to the west by MTD and to the east by infill sediments within the Danube Channel. Infill sediments, unlike levee accumulations, do not exhibit regular stacking, and no BSR is observed within them. In the “Z” area, both “BSR1” and “BSR2” reflections are within unit number 8. This unit does not contain any channel structure. The MTD structure within the “Z” area has affected the continuity of BSR1 and BSR2 reflections in some areas, forming the distribution map shown in Figure 2. All primary and multiple BSRs in the study area have developed within units 7, 8, and 10: BSRs only formed within specific units; and none of the BSRs intersect another unit.

2.4. The Relationship Between MTDs and BSR

The study area contains various MTD structures. Some are small-scale MTDs, while others extend over hundreds of square kilometers. Considering that BSRs are observed at depths between 2000 and 2700 ms, the interpretation of MTD structures at these depths is particularly important. These MTD structures within the gas hydrate stability zone have been numbered from 1 to 6 (Figure 5). The table below provides the surface areas and maximum thickness values for each of these MTDs (Table 2).

Table 2- Areas and Maximum Thicknesses of MTD Structures within the Gas Hydrate Stability Zone.

MTD Number	Area (km^2)	Maximum Thickness (m)
MTD_1	1220	200
MTD_2	2440	500
MTD_3	255	105
MTD_4	1200	180
MTD_5	60	45
MTD_6	420	70

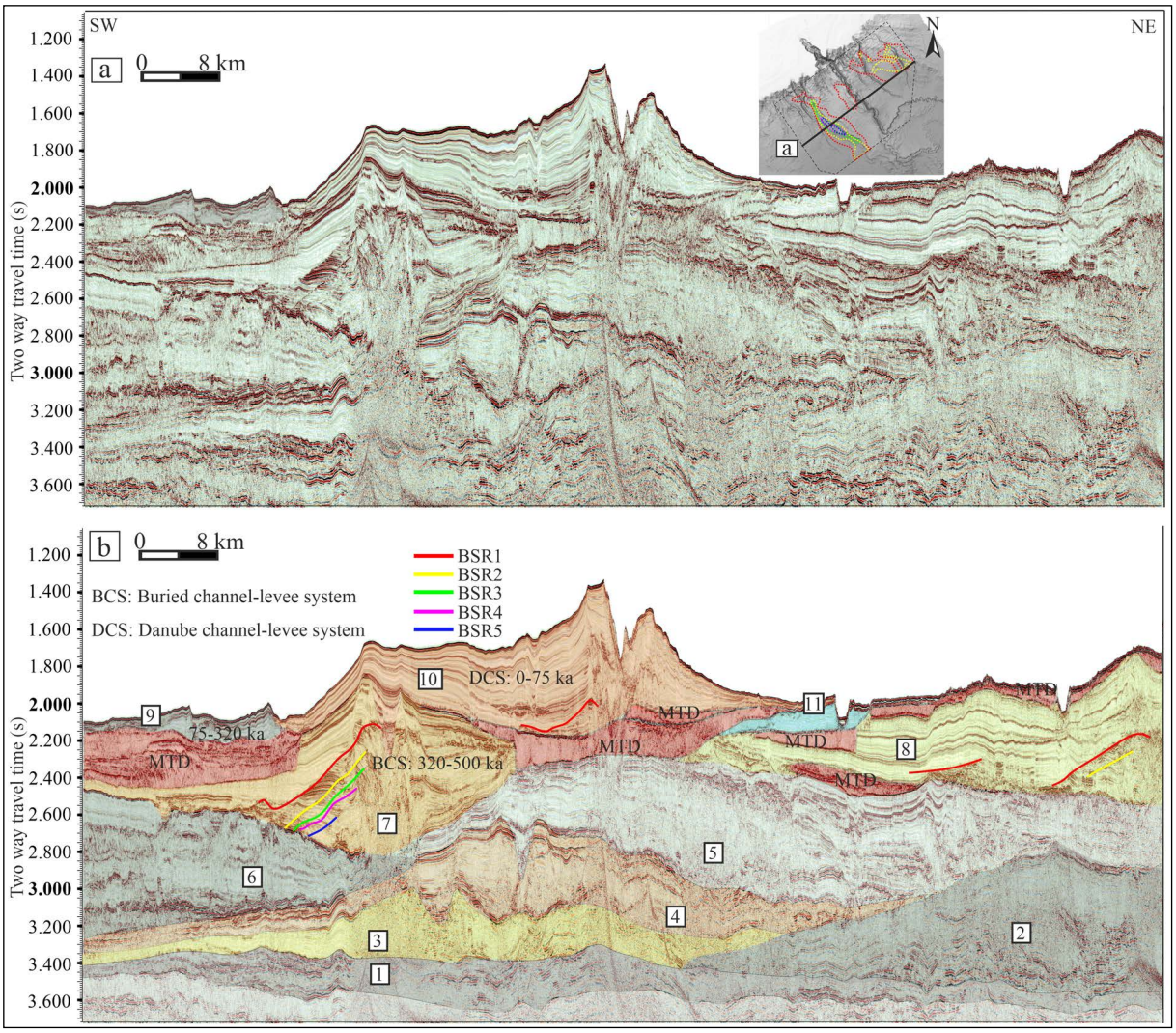

Figure 4- a) A sample seismic section intersecting all three BSR areas, b) The interpreted version of the seismic section. Different seismic units observed in the section are numbered from 1 to 11. MTD represents mass transport deposits. Details are provided in the text.

MTD_1, located at the westernmost part of the area, extends in a manner that delineates the western boundary of the BSR area known as "X." Within the gas hydrate stability zone of the "X" area, MTD_1 is the second-largest MTD structure The MTD_2 structure, found at the base of the current channel-levee system, is also within the gas hydrate stability zone of the "X" area. However, MTD_2 is located beneath the BSRs in the "Y" area. The southern ends of the BSRs comprising the "Y" area terminate above MTD_2. Additionally, as seen in Figure 5, MTD_2, similar to MTD_1, delineates the eastern boundary of the "X" area from the east, indicating that the "X" area is constrained by MTD structures.

MTD_3 is located at the base of the eastern flank of the current channel-levee system and has no contact with any BSR. This smaller mass movement is entirely comprised within the study area and has no relationship with any BSR area (Figure 5a). MTD_4, the third-largest MTD mapped in terms of area, is closest to the seafloor. It is quite shallow, and thus, it has no relationship with any BSR in the study area (Figure 5d). MTD_5 intersects with the reflections in the "Z" BSR area and divides the area into two parts, known as "Z1" and "Z2." MTD_5 is the smallest mapped mass transport deposit in terms of area within the gas hydrate stability zone (Figure 5b). MTD_6 is directly associated with the "Z1" BSR area. In this region, the western ends of the BSRs terminate

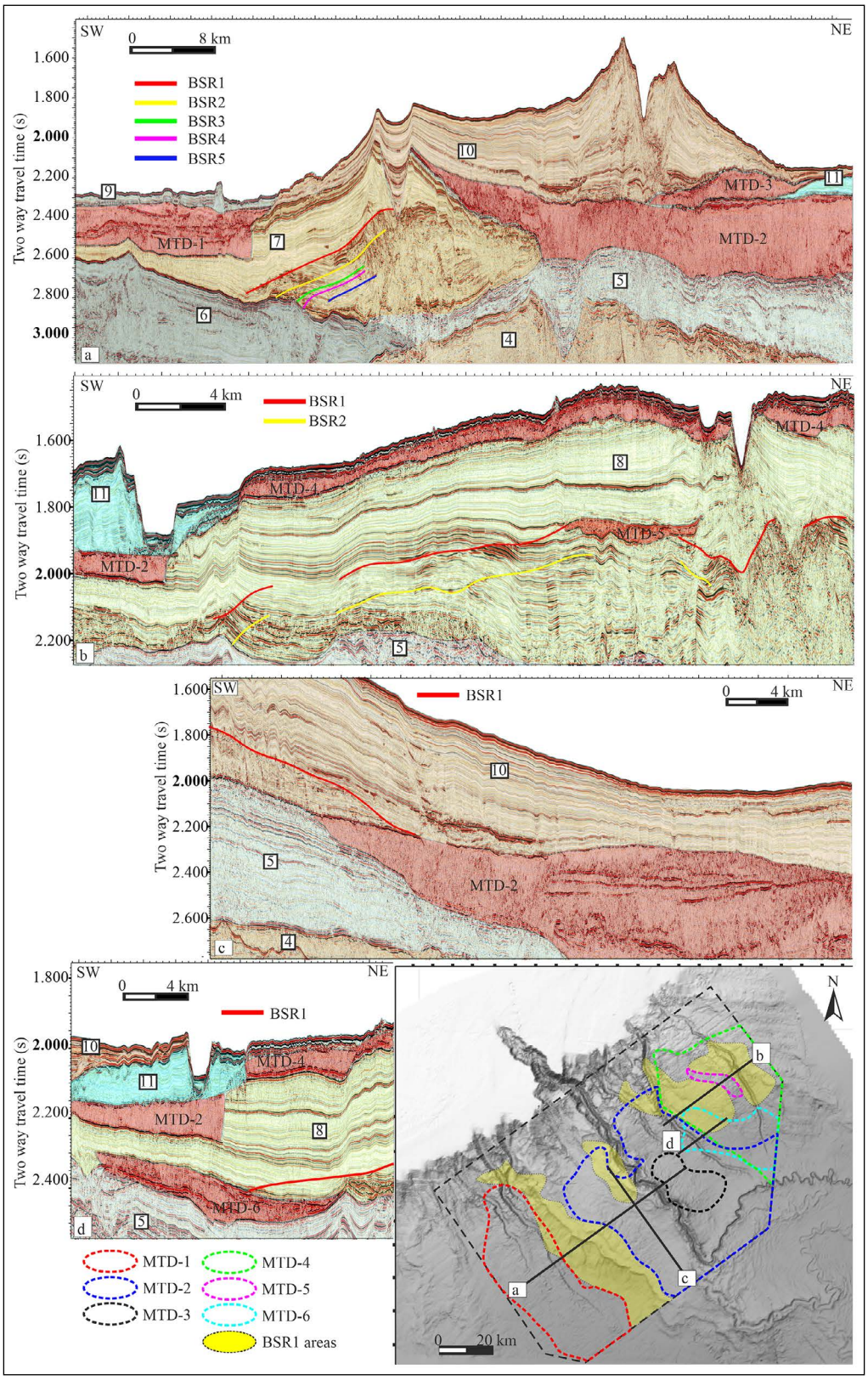

Figure 5- Examples of MTDs in the study area from seismic sections and their distribution, a) MTD structures observed in a sample seismic section in the "X" BSR area, b) MTD structures observed in a sample seismic section in the "Z" BSR area, c) MTD structures observed in a sample seismic section in the "Y" BSR area, d) another example of a seismic section showing MTD structures in the "Z" BSR area. 6 MTD structures within the gas hydrate stability zone have been interpreted in the area.

within the MTD_5 mass transport deposit (Figure 5d). Although the "Z1" area on the map does not appear to be bounded by MTD_6, the terminations of reflections on the mass transport deposit can be observed in the seismic sections in Figure 5. While many small-scale mass transport deposits were observed both within the stability zone and in deeper regions within the study area, the study only interpreted mass transport deposits that were associated with BSRs and demonstrated continuity in other profiles.

2.5. Seismic Attributes Analysis

To highlight the differences in amplitudes between BSRs and the underlying free gas anomalies, envelope calculations were applied to all profiles, without the use of any gain process. As an example, seismic sections from the "X, Y, and Z" BSR areas are shown in Figure 6. In addition, an instantaneous frequency attribute analysis was applied to emphasize low-frequency zones in gas-bearing units. Since only Type 1 BSR reflections were observed a, indicating the presence of free gas below the BSR levels was not possible, while instantaneous frequency attribute analysis was applied to all BSR areas, no anomalies related to frequency were observed in the sections.

Figures 6a and 6b depict seismic sections as examples in the region with multiple BSRs consisting of 5 layers within the "X" area. In this area, the high amplitudes at the boundaries of BSR_1 and BSR_2 continue along the BSR level. The reflections beneath the BSR_1 level exhibit amplitudes approximately four times higher than those above, and these high amplitudes are located between the BSR_1 and BSR_2 levels.

Throughout the entire "X" area, the high-amplitude reflections are all located between the BSR_1 and BSR_2 levels. In the "Y" BSR area, no multiple BSRs are observed. An analysis was conducted on a line that cuts across the area in a north-south direction to examine the reflection amplitudes. That analysis reveals that the BSR level did not produce high-amplitude anomalies on the envelope section (Figure 6d). Consequently, no amplitude difference that can be compared either above or below the BSR was formed.

The "Z" BSR area, as seen in Figure 5b, is divided by the MTD structure, and both sides exhibit BSR_2. Therefore, this area is exemplified with two different envelope sections. In Figure 6f, in the area north of the "Z1" BSR area where multiple BSRs are present, high-amplitude anomalies were observed along the BSR_1 line. The amplitudes below the BSR_1 line are approximately 10 times higher than the amplitudes above, and all high amplitudes are observed between the two BSRs, just as in the "X" area. The amplitudes of BSR_2 in this area did not create high-amplitude anomalies in the form of a line, and there are no high-amplitude reflections below the BSR level. In addition, in the section shown in Figure 6f, high-amplitude reflections are continuing to the west of the BSR, even though BSRs are not observed. The amplitudes of the reflections below the BSR are approximately 10 times higher than those above. Finally, in the envelope section of the seismic line that separates the BSR area with the MTD shown in Figure 6h, when examining the reflection amplitudes in the region with both multiple and single BSRs, it is observed that the high-amplitude reflections below the BSR are approximately 30 times higher than the reflections above the BSR. There are no multiple BSRs below the BSR to the west of the section, and the high-amplitude reflections in this area continue until the MTD structure in the middle of the "Z" area. In the area to the east of the MTD, as in the "X" area, high-amplitude reflections are observed between the two BSRs (Figure 6h). Therefore, all high-amplitude reflections in the multiple BSR areas are located between the BSR_1 and BSR_2 reflections.

2.6. Calculated Phase Equilibria for Gas Hydrates

2.6.1. Phase Equilibrium for Gas Hydrate Composed Solely of Methane

To calculate the gas hydrate phase equilibrium for BSR levels, a depth migration process was used to convert two seismic profiles to depth sections for the "X" and "Z" regions. When the equilibrium curve for gas hydrates was computed for a selected point at the center of the BSR region intersected by the east-west seismic line (Figure 7a), the curve shown by the blue line in Figure 7a was obtained. Upon comparison

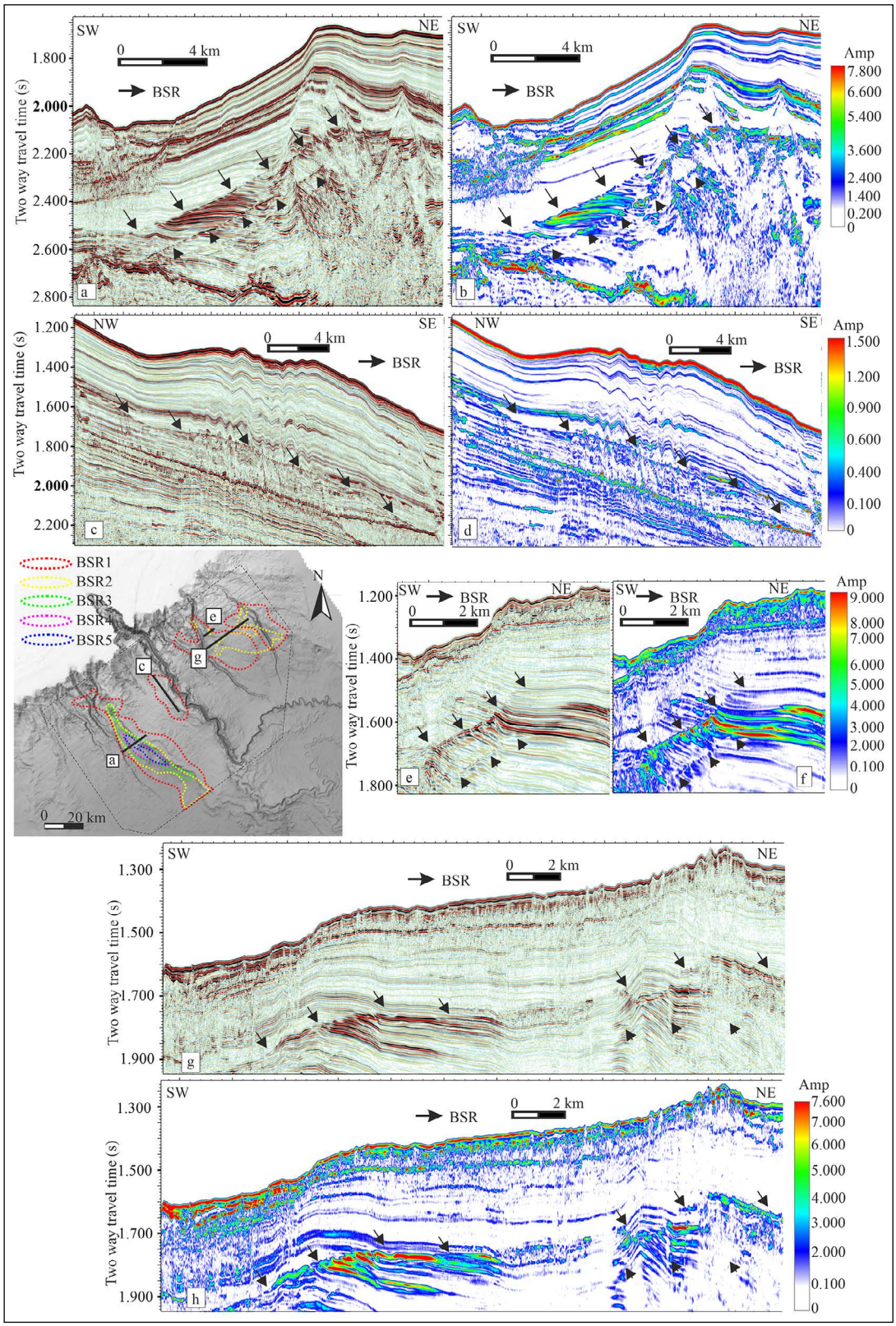

Figure 6- Samples of seismic sections containing BSRs in the study area and envelope sections created from instantaneous attribute analysis applied to these sections, a) Sample seismic section from the "X" BSR area and b) the envelope image of this section, c) Sample seismic section from the "Y" BSR area and d) the envelope image of this section, e) Sample seismic section from the "Z1" BSR area and f) the envelope image of this section, g) Sample seismic section from the "Z" BSR area and h) the envelope image of this section. Envelope sections show high-amplitude anomalies beneath BSR1 in the "X" and "Z" BSR areas.

of this curve with the depth of the BSR obtained from the seismic section, the regional temperature gradient calculated for gas hydrates consisting solely of methane is approximately 24.5°C/km. This temperature gradient is lower compared to the gradients in other studies (30°C/km; Vassilev and Dimitrov, 2003; Popescu et al., 2006). At this point, the BSR depth is 1750 meters, with a seabed depth of 1410 meters. With a 340-meter BSR thickness, and a temperature at the seabed of 9°C, the temperature at the BSR level on the equilibrium curve corresponds to approximately 17.3°C. The 24.5°C geothermal gradient value obtained from the curve, assuming 100% methane content, was also used in another BSR area, the "Z" area, and an equilibrium curve was calculated (Figure 7b).

In the region to the north of the S3 channel, east of the Danube Channel, the seabed depth is 880 meters, and the BSR depth is 1040 m. Compared to the BSR depth in Figure 7a, the BSR thickness in this region is 180 m less than the BSR thickness in the deep area. For this region where the thickness of the BSR is less than half, the equilibrium curve calculated based on methane and a geothermal gradient of 24.5°C/km precisely coincides with the curve at the BSR level (Figure 7b). In the region with a 160 m BSR thickness, the temperature at the BSR level on the equilibrium curve is approximately 12.9°C. Using the same geothermal gradient, the seismic section that crosses the "Y" BSR area in a north-south direction clearly shows that BSR thicknesses increase downslope

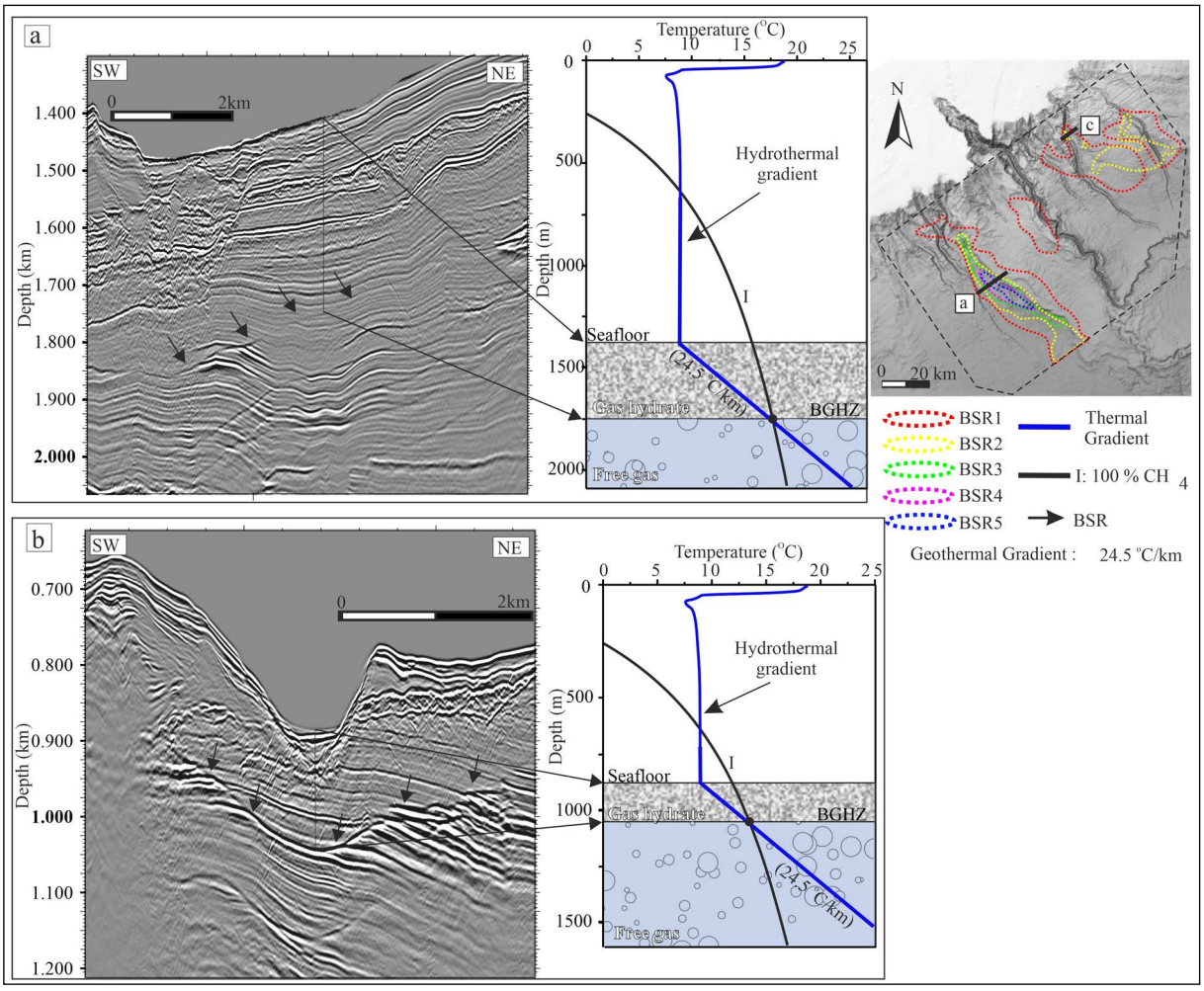

Figure 7- Theoretical gas hydrate stability curve generated from two sample seismic sections with depth migration applied in the "X" and "Z1" BSR areas. The equilibrium curve calculated for a geothermal gradient of 24.50°C/km in both seismic sections intersects at the BGHSZ point with the curve created for 100% methane.

as BSRs occur at different depths and thicknesses (Figure 3d).

2.6.2. BSR Irregularities and Heat Flow Variations

The BSRs observed in seismic sections presumably follow isothermal contours. These isothermal contours are generally controlled by the gas composition that forms gas hydrates. For a constant heat flow value, it can be assumed that the isothermal level extends parallel to the seafloor at a constant depth below the seafloor. Therefore, BSR levels extend parallel to the seafloor and intersect the stratigraphic layers in seismic sections. However, there are instances when the BSR level doesn't extend parallel to the seafloor and irregularities occur at BSR depth. This is often associated with local variations in geothermal gradients. Ome irregularities in BSR levels have also been observed in the study area. These irregularities have been analyzed taking into account heat flow measurement values in the area.

Heat flow measurements made in the region where multiple BSRs are observed in the "X" BSR area are shown in Figure 8. Geothermal gradient values obtained from 8 heat flow measurements, are shown on BSR for each point, and the BSR depths at these points have been calculated (Figure 8b).

When looking at the heat flow measurements from HF_1 to HF_8, it is observed that the BSR thicknesses at these points reach up to 350 m, extending into the region with the MTD structure. The BSR thickness values at the other measurement points increase eastward starting from the western boundary of the MTD structure. There is a 30 m thickness difference between the westernmost measurement point and the easternmost measurement point. The BGHSZ level corresponding to the previously calculated geothermal gradient of 24.5°C/km is shown by the yellow dashed line, and the actual BSR reflection (purple line) is deeper than the calculated yellow line gradient exactly where the western boundary of the MTD is located, and this difference has increased gradually. The reflection characteristics of the BSR in Figure 8b, which is not exactly parallel to the seafloor, are also seen in Figure 8c. For this profile, the loss of parallelism starts with the eastern boundary of the MTD. Looking at the geothermal gradient values, the values inside and outside the MTD structure should be evaluated. The geothermal gradient values in the MTD structure section are likely higher compared to those outside the MTD structure (Figure 8a).

3. Discussions

3.1. Distribution and Characteristic Features of BSRs

The presence of BSRs in the study area was initially established through seismic studies conducted by Popescu et al. (2006). While the three mapped BSR areas within the study area (Figure 2) exhibit similarities to the proposed BSR distribution map by Popescu et al. (2006), the suggested BSR distribution and its characteristic features in this study exhibit both spatial and stratigraphic differences. The shallowest water depth where BSRs were observed is 665 m, and this depth has been calculated as the minimum depth for the possible occurrence of gas hydrates in the region (for methane-only gas hydrates). This depth limit is consistent with the minimum limit calculated by Zander et al. (2017) as 665 m. Popescu et al. (2006) interpreted two BSR areas to the east and west of the Danube Channel, but seismic data shows that there is another BSR area spread over an area of 172 km² to the west of the channel (Figures 3c, d). The higher density of seismic lines used in this study, along with the use of a seismic system with a wider frequency band and smaller group interval, has resulted in higher seismic data resolution compared to the seismic sections provided by Popescu et al. (2006). Therefore, although the multiple BSRs in their "B" BSR area are consistent with our results, no multiple BSRs were observed in the seismic section within the "C" area. However, this study clearly reveals the presence of multiple BSRs in the area referred to as "Z" (Figure 3d).

Hyndman and Davis (1992) categorized the reflection characteristics of BSRs into two separate types.. The first class consists of BSRs with consistent reflection amplitude that continues lateraly. These reflections are referred to as Type 1 reflections, and they do not imply the presence of free gas below the BSR level (Özel et al., 2022). The second class includes reflections that terminate at the BSR level

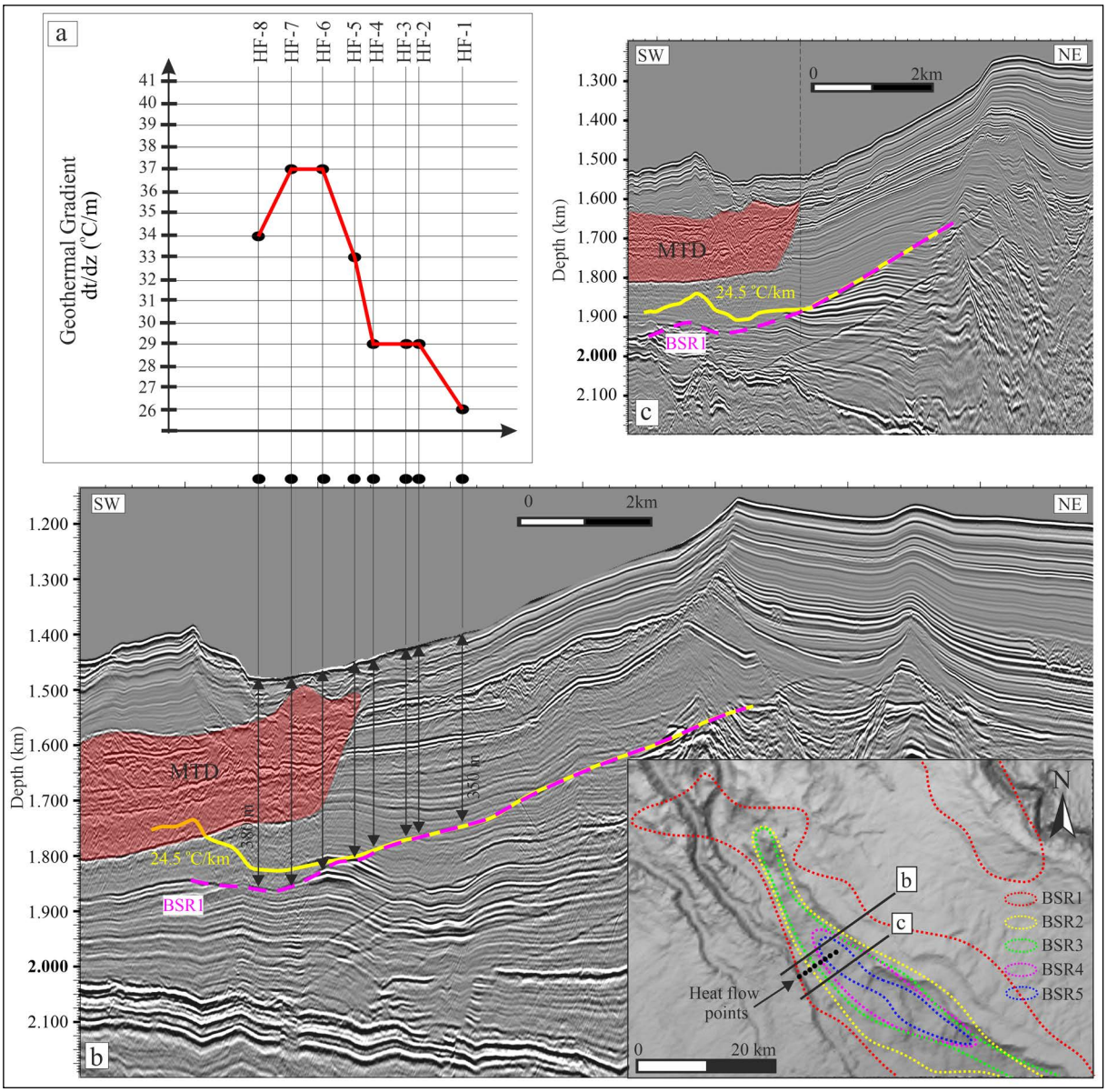

Figure 8- Geothermal gradient values from heat flow measurements (HF points) conducted in the "X" BSR area and their locations on sample seismic sections, a) Geothermal gradient values obtained from eight heat flow measurements, half of which correspond to the MTD structure. b) Image of a sample seismic section located to the north of the "HF" points and the positions of "HF" points on the section. c) Image of a sample seismic section located to the south of the "HF" points and the positions of "HF" points on the section. The geothermal gradient values obtained from heat flow measurements on the MTD_1 structure in the westernmost part of the study area were observed to be higher than measurements at other points in the same region. The yellow line represents the BSR level drawn for a geothermal gradient of 24.50°C/km. The purple dashed line corresponds to the observed BSR1 level.

and are characterized by high amplitudes, which indicate the presence of free gas below the BSR level. These are referred to as Type 2 reflections. Based on the reflection characteristics in Hyndman and Davis's (1992) BSR definition, Type 1 BSRs are observed throughout the study area. Since there are no gas seeps or mud volcanoes associated with faults in the area, it is believed that all BSRs in the area developed consistently in line with Type 1 characteristics.

In the western part of the study area, within the "X" BSR area, despite the presence of free gas in the acoustic turbidity zone, Type 1 BSRs are not observed (Figures 3a, b). This is because the acoustic turbidity zone in the northern part of the area is deeper than

the BSR level. Although the acoustic turbidity zone is within the BSR area, it does not create Type 2 BSRs. In fact The gas accumulation in this area, especially north of the "X" area, terminates well below the BSR stability zone. Turbidity, and for a BSR to exhibit Type 2 reflection characteristics, the gas accumulation must reach the BSR level. In this case, it can be said that Type 2 BSR behaves as a cap layer that allows free gas accumulations beneath it.

3.2. Units Without BSR

The absence of Bottom Simulating Reflectors (BSR) in the study area can be attributed to several factors. The distribution and characteristics of gas hydrate accumulations are directly influenced by various geological features within the BSR stability zone. The properties of gas hydrate accumulations are dependent on the physical characteristics of the stratigraphic units in which they are located, in addition to temperature and pressure conditions. One significant factor affecting the characteristics of gas hydrate accumulations in the study area is the presence of MTD structures. These MTD structures exhibit different physical properties compared to other geological features within the BSR stability zone. The study area contains various stratigraphic units, paleo-channels, units responsible for acoustic turbidity, and MTDs, all of which have distinct physical properties (Figure 4).

MTD structures can extend over areas as large as 2440 km^2 (Figure 5). Some of these MTDs, such as MTD_1, MTD_2, and MTD_6, are entirely located beneath BSR levels. MTD_5, although the smallest of the MTDs, intersects with a BSR level. In regions where MTDs beneath the BSR level are observed, or where they extend above or below the BSR level, BSRs are still present in the seismic sections. Nasıf et al. (2020) noted that BSRs exist beneath MTD structures in the Sakarya Canyon offshore, but no BSRs were observed above the MTD structures. They suggested that this could be due to the upward migration of gas that forms gas hydrates and the obstruction of gas flow by MTD structures located in deeper layers.

In the case of the "Y" and "Z" BSR areas, the largest-scale MTD structure is found below the "Y" area's BSR. Therefore, it seems unlikely that gas hydrates in the "Y" area would be supplied by free gas below the BSR level. The "Z" area, especially in the southwest, contains MTD_6, which is positioned just below the BSR level, similar to MTD_2 beneath the "Y" area. Despite the absence of free gas accumulation below or around it, BSRs have formed in this region (Figure 5).

Another MTD structure within the "Z" area, MTD_5, is present, and no BSR is observed within this MTD or any of the MTDs within the entire study area. The reason for this may be that, as demonstrated by several studies (Dugan, 2012; Reece et al., 2012; Hornbach et al., 2015; Sun et al., 2018; Nasıf et al., 2020; Sun and Alves, 2020), MTDs typically have high density, low porosity, low water content, and low permeability compared to surrounding sediments. During the formation and burial of MTDs, the over-consolidation of the sliding material hinders vertical fluid and gas migration, preventing the formation of gas hydrates within these structures. In conclusion, it is suggested that gas hydrate formation is not possible within MTDs, and there is no apparent relationship between the presence of gas hydrates either beneath or above areas with MTD structures.

Another unit within the stability zone where BSR is not observed is Unit 6 (Figure 4). All reflections in the "X" BSR area terminate to the east of Unit 6. Although the shallow parts of this unit are within the gas hydrate stability zone, all BSRs in the region end at the boundaries of Units 6 and 7. The reason for this might be the physical properties of the sediments comprising Unit 6, such as low porosity, and low permeability, which could differ from the units where BSR is observed. Additionally, the difference in physical properties within Unit 6 might be due to its channel-levee system being fed from a different source outside and to the west of the study area3.

3.3. Heat Flow-MTD Relationship

In the "X" BSR area, the BSRs observed tend to mimic the seafloor, but this characteristic fades as you move eastward. In the eastern part, the depth from the seafloor to the BSR level is 350 m, while in the far west, the observed BSR depth has reached up to 380 m

(Figure 8b). Zander et al. (2017) attributed the depth discrepancy between the theoretically calculated BSR level based on a 24.5°C/km geothermal gradient (yellow line) and the observed actual BSR level (purple line) in this region to the unstable nature of the area and suggested that this instability results from rapid levee accumulation.

In this study, it is considered that the irregularity in BSR depth in the region is due to MTD-related factors. The point at which the theoretically calculated BSR level and the actual BSR level diverge corresponds precisely to the location where the MTD structure is observed. The geothermal gradients (dt/dz) obtained from heat flow measurements HF-5-6-7-8 within the MTD boundaries, starting from the eastern boundary of MTD_1 and located within the MTD boundaries, are higher compared to those outside the MTD boundaries. This indicates that the sediment within the MTD boundaries has a higher thermal conductivity than the sediments outside the MTD boundaries (Figure 8a). Given that the MTDs have lower porosities and permeabilities compared to the surrounding sediments, it is possible that the thermal conductivities of the sediments composing the MTD structures are higher. This interpretation aligns with a study by Zhang et al. (2022), which showed that sediments with low porosity and high temperatures have higher thermal conductivities. This presumably thermal conductivity of the MTD structures would allow heat to be conducted more easily in the sediments containing gas hydrates . In turns, this would explain why the BSR has been observed at a depth deeper than it should be, and there is an approximately 30 m difference between the yellow line calculated based on the 24.5°C/km geothermal gradient and the actual (purple) BSR level in Figure 8b.

3.4. Causes of Multiple BSRs

In the world's oceans, multiple BSRs have been observed in a few areas, as documented by studies such as Foucher et al. (2002) and Zhang et al. (2022). In all of these areas, a single paleo-BSR level extending below the current BSR level has been observed. The Danube Delta is the first and only region in the world where five stacked BSR levels have been observed simultaneously, believed to be directly related to levee systems. These BSRs were first reported by Popescu et al. (2006).

There are two areas in the study region where multiple BSRs have been observed. The first is the "X" BSR area, which contains BSRs consisting of five levels. The second is the "Z" BSR area, which contains BSRs consisting of two levels (Figures 2 and 3). The theories regarding the formation of multiple BSRs, which are still a subject of debate, are also applicable to this region. One possible explanation is that different gas compositions directly affect the depths at which BSRs form. Regions with gas hydrate accumulations containing varying proportions of thermogenic gases (such as ethane, propane, butane, etc.) within largely methane-based gas hydrates can exhibit multiple stacked BSRs since the composition of gases influences the BSR level on the phase equilibrium curve.

Popescu et al. (2006) proposed the idea that different gas compositions might be one of the reasons for the formation of multiple BSRs in the same region. In the "Z" BSR area located to the east of the study region, a gas chromatography analysis of a 147 m core sample taken from multiple BSRs by Pape et al. (2020) revealed trace amounts of thermogenic gases. Furthermore, in another study conducted in the same area, Chazallon et al. (2021) reported that a core sample consisting of 99.5571% methane, 0.0071% ethane, and 0.0002% propane was found in the chromatography results. However, because the ratios of heavier hydrocarbon gases in these samples are significantly lower than the values required for the formation of multiple BSRs with different gas compositions in the region. It appears challenging to attribute the formation of multiple BSRs in the "Z" study area to different gas compositions. Nonetheless, obtaining a core sample from the "X" area that extends down to the BSR level will provide the most accurate answer and help clarify the reasons for the formation of multiple BSRs in this specific region.

Another potential explanation for the formation of multiple BSRs in the study area could be the sedimentation rate in the region being higher than the rate at which gas hydrates dissolve. To express this concept, a conceptual model is provided in Figure 9.

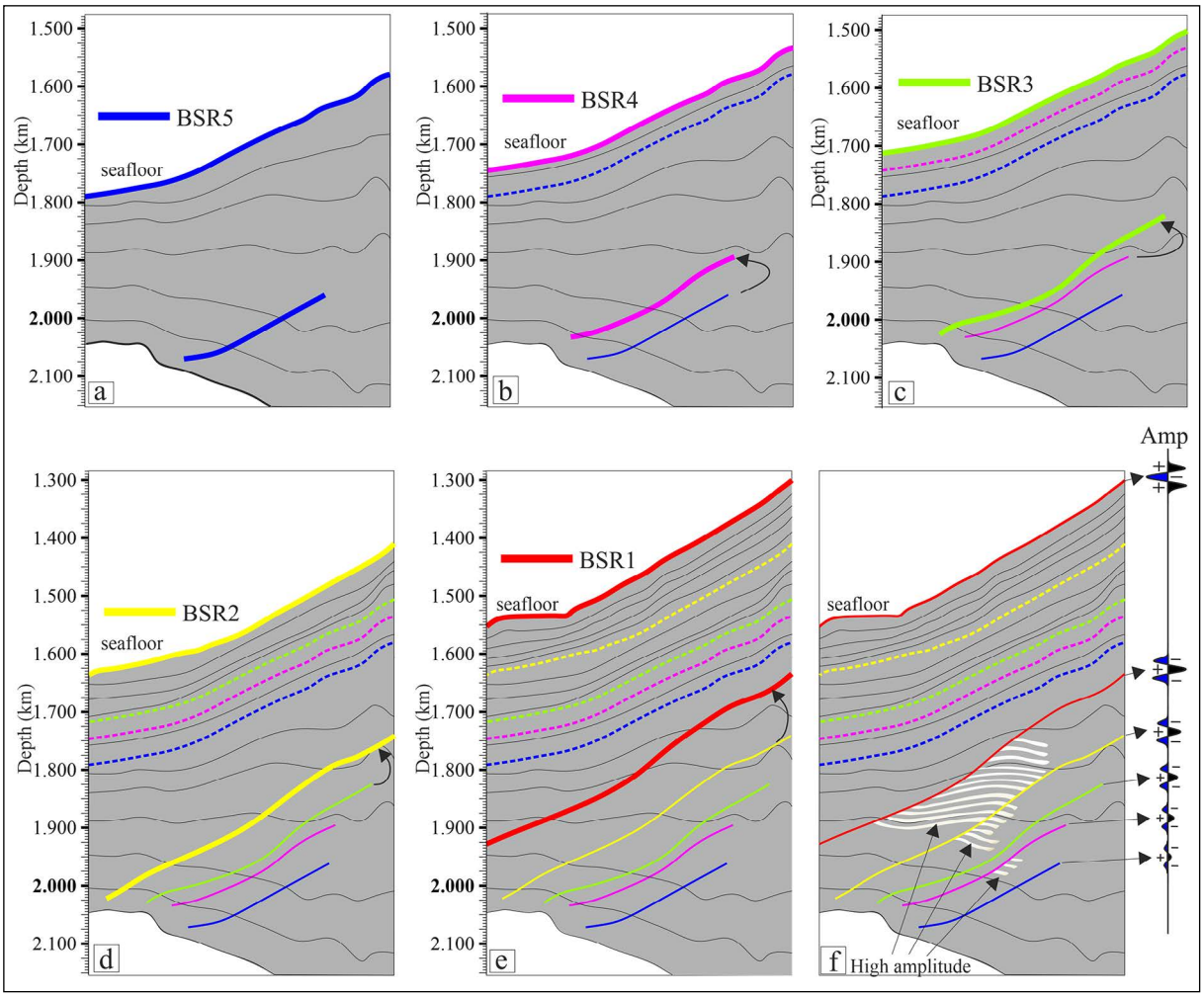

Figure 9- A conceptual model explaining the formation mechanism of multiple BSRs showing successive snapshots from a) to e), as sediments rapidly accumulate at the seafloor, f) Model explaining high-amplitude reflections associated with gas developed between BSR levels and the decreasing amplitudes of BSR levels from BSR5 to BSR1. Due to the higher sedimentation rate in the area compared to the gas hydrate dissociation rate, the BSRs rise from level 5 to level 1, but because gas hydrate dissociation continues, both multiple BSRs are observed, and high-amplitude reflections have developed between BSR levels due to free gas in the environment.

Zander et al. (2017) demonstrated that the stability zone of BSR levels in the "X" BSR area developed in accordance with paleo-sea floor levels. Although they suggested that the gas responsible for forming the BSR levels would not migrate vertically, it is challenging to provide another explanation for why the BSR levels, consisting of five levels, are still visible in seismic sections. In areas with rapid sedimentation, BSR levels are expected to migrate upward. However, the presence of deeper paleo-BSRs in seismic sections may be evidence that gas hydrate dissociation is ongoing. Particularly, the presence of free gas between BSR1 and BSR2 levels, clearly seen in Figure 6b with high amplitudes in envelope sections, supports this argument. Furthermore, the decreasing amplitudes on top of the BSRs from BSR1 to BSR5 may also indicate that the gas concentration in the region decreases with depth. In this case, the gas dissolving at the paleo-BSR level may, contrary to Zander et al. (2017) claim, migrate vertically, accumulating below the BSR level in shallower parts of the field and/or forming new BSRs in shallower areas.

The endothermic nature of gas hydrate dissociation reactions means that they cool the surrounding environment during the dissociation process. This cooling effect, occurring as hydrates dissolve, may extend the dissociation process and help explain why multiple BSRs continue to exist in the region beyond

the depths where they reach equilibrium. The fact that BSR5 has a significantly lower amplitude while BSR1 has a higher amplitude, coupled with the ongoing dissociation, suggests that, given the sedimentation rate in the environment, additional multiple BSRs may form in the future, so that BSR1, which is currently the uppermost, could become a secondary BSR level. The formation of multiple BSRs in the "Z" BSR area, consisting of only two levels, is also believed to be related to the lower sedimentation rate in the region.

As shown in Figure 4, it is apparent that the units of levee banks generally accumulate to the west of the study area. The contemporary Danube Channel, formed by sediments of the western wing of the levee banks extending further westward, indicates a higher sedimentation rate in this region compared to the east. Therefore, the lower sedimentation rate in the "Z" BSR area compared to the "X" BSR area located to the west may have limited the formation of multiple BSRs to only two levels in the former.

4. Results

Seismic reflection data document that the study area is rich in gas hydrates. The BSRs are distributed across three zones: the western "X" BSR area covering 825 km^2, the central "Y" BSR area covering 172 km^2, and the eastern "Z" BSR area, which is further divided into two parts, totaling 710 km^2. All the BSR types in these areas are composed of reflections known as Type-1, which intersect layers and exhibit continuous reflection characteristics. Multiple BSRs are observed, with the "X" area having five levels and the "Z" area having two levels.

Within the BSR stability zone, there are six MTD structures, and no BSRs have been observed within any of these MTD structures. We propose that gas hydrates did not form within these structures due to the excessive consolidation of the MTD material during their formation. Heat flow measurements taken from the "X" BSR area show that the geothermal gradients above the MTD structure are higher compared to other areas. Suggesting that the MTD has a higher thermal conductivity. Therefore, due to the more easily conducted heat, the depth at which BSR reaches equilibrium is observed deeper than expected.

Given the presence of only trace amounts of heavy gases in core samples from the "Z" BSR area, it is difficult to attribute the formation of BSRs in this area to different gas compositions. A more likely reason for the multiple BSRs may be the sedimentation rate being higher than the rate of gas hydrate dissociation. The fact that the lowermost BSR level, has the lowest amplitude while the uppermost BSR level has the highest amplitude supports this idea. Additionally, the presence of free gas between the first and second BSR levels is an indication that dissociation is still on going.

Acknowledgment

We would like to express our gratitude to the GEOMAR Helmholtz Centre for Ocean Research Kiel Institute for their contributions in data collection under the SUGAR Project. Special thanks to the SeisLab geophysics laboratory team within the Institute of Marine Sciences and Technology. We also extend our appreciation to the scientific team aboard the R/V MARIA S. MERIAN research vessel and the ship's crew for their dedicated efforts during the data collection process. We would like to acknowledge SEAMAP Inc. for their technical support in providing the equipment used in the laboratory during data collection. Additionally, we are grateful to the State Planning Organization for their support under project code "2003K120360," which was instrumental in procuring the equipment and establishing the data processing laboratory. We also want to express our thanks to Landmark Graphics for providing the SeisSpace/Promax seismic data processing software. Lastly, we extend my appreciation to IHS Markit for generously providing the Kingdom Suite software for the interpretation of seismic data.

References

Andreassen, K., Mienert, J., Bryn, P., Singh, S. C. 2000. A Double gas-hydrate related bottom simulating reflector at the Norwegian continental margin. Annals of the New York Academy of Sciences, 912(1), 126–135.

Andreassen, K., Nilssen, E. G., Ødegaard, C. M. 2007. Analysis of shallow gas and fluid migration within the Plio-Pleistocene sedimentary succession of the SW Barents Sea continental margin using

3D seismic data. Geo-Marine Letters, 27(2–4), 155–171.

Ashi, J., Tokuyama, H., Taira, A. 2002. Distribution of methane hydrate BSRs and its implication for the prism growth in the Nankai Trough. Marine Geology, 187(1–2), 177–191.

Baba, K., Yamada, Y. 2004. BSRs and Associated Reflections as an Indicator of Gas Hydrate and Free Gas Accumulation: An Example of Accretionary Prism and Forearc Basin System along the Nankai Trough, off Central Japan. Resource Geology, 54(1), 11–24.

Bangs, N. L. B. 2005. Upward shifts in the southern Hydrate Ridge gas hydrate stability zone following postglacial warming, offshore Oregon. Journal of Geophysical Research, 110(B3).

Bangs, N. L., Hornbach, M. J., Berndt, C. 2011. The mechanics of intermittent methane venting at South Hydrate Ridge inferred from 4D seismic surveying. Earth and Planetary Science Letters, 310(1–2), 105–112.

Belousov, V. V., Volvovsky, B. S. 1989. Structure and Evolution of the Earths's Crust and Upper Mantle of the Black Sea, Nauka, Moscow (in Russian).

Bialas, J., Klaucke, I., Haeckel, M. 2014. Fs Maria S. Merian Fahrtbericht / Cruise ReportMSM34/1 & 2 - SUGAR Site; Varna – Varna.

Chazallon, B., Rodriguez, C., Ruffine, L., Carpentier, Y., Donval, J. P., Ker, S., Riboulot, V. 2021. Characterizing the variability of natural gas hydrate composition from a selected site of the Western Black Sea, off Romania. Marine and Petroleum Geology, 124, 104785.

Cook, A. E., Goldberg, D. S., Malinverno, A. 2014. Natural gas hydrates occupying fractures: A focus on non-vent sites on the Indian continental margin and the northern Gulf of Mexico. Marine and Petroleum Geology, 58, 278–291.

Çifci, G. 2020. Gas hydrates: The energy source of the near future. Belt and Road Initiative Quarterly, 2(1), 63-76.

Dondurur, D. 2021. Gaz Hidratlar ve Çevre Denizlerimizde Gaz Hidrat Potansiyeli, Türkiye'nin Ekstrem Deniz Araştırmaları Ortamları. Türk Deniz Araştırmaları Vakfı (TÜDAV), 2021, 52-75.

Du Fornel, E. 1999. Architecture du cône profond du Danube ensismique reflexion 2D. MSc dissertation Université Montpellier II: 46 pp.

Dugan, B. 2012. Petrophysical and consolidation behavior of mass transport deposits from the northern Gulf of Mexico, IODP Expedition 308. Marine Geology, 315–318, 98–107.

Finetti, I., Bricchi, G., Del Ben, A., Pipan, M., Xuan, Z. 1988. Geophysical study of the Black Sea. Bolletino Di Geofisica Teorica Ed Applicata, 30, 197–324.

Foucher, J. P., Nouzé, H., Henry, P. 2002. Observation and tentative interpretation of a double BSR on the Nankai slope. Marine Geology, 187(1–2), 161–175.

Ginsburg, G. D. 1998. Submarine Gas Hydrates. VNIIOkeangeologia.

Haacke, R. R., Westbrook, G. K., Hyndman, R. D. 2007. Gas hydrate, fluid flow and free gas: Formation of the bottom-simulating reflector. Earth and Planetary Science Letters, 261(3–4), 407–420.

Hillman, J. I., Klaucke, I., Bialas, J., Feldman, H., Drexler, T., Awwiller, D., Atgin, O., Çifçi, G., Badhani, S. 2018. Gas migration pathways and slope failures in the Danube Fan, Black Sea. Marine and Petroleum Geology, 92, 1069–1084.

Holbrook, W. S., Hoskins, H., Wood, W. T., Stephen, R. A., Lizarralde, D. 1996. Methane Hydrate and Free Gas on the Blake Ridge from Vertical Seismic Profiling. Science, 273(5283), 1840–1843.

Hornbach, M. J., Manga, M., Genecov, M., Valdez, R., Miller, P., Saffer, D., Adelstein, E., Lafuerza, S., Adachi, T., Breitkreuz, C., Jutzeler, M., Le Friant, A., Ishizuka, O., Morgan, S., Slagle, A., Talling, P. J., Fraass, A., Watt, S. F. L., Stroncik, N. A., Wang, F. 2015. Permeability and pressure measurements in Lesser Antilles submarine slides: Evidence for pressure-driven slow-slip failure. Journal of Geophysical Research: Solid Earth, 120(12), 7986–8011.

Horozal, Ş., Lee, G. H., Yi, B. Y., Yoo, D. G., Park, K. P., Lee, H. Y., Kim, W., Kim, H. J., Lee, K. 2009. Seismic indicators of gas hydrate and associated gas in the Ulleung Basin, East Sea (Japan Sea) and implications of heat flows derived from depths of the bottom-simulating reflector. Marine Geology, 258(1–4), 126–138.

Hyndman, R. D., Davis, E. E. 1992. A mechanism for the formation of methane hydrate and seafloor bottom-simulating reflectors by vertical fluid expulsion. Journal of Geophysical Research: Solid Earth, 97(B5), 7025–7041.

Ivanov, M., Limonov, A., van Weering, T. 1996. Comparative characteristics of the Black Sea and Mediterranean Ridge mud volcanoes. Marine Geology, 132(1–4), 253–271.

Kazmin, V. G., Schreider, A. A., Bulychev, A. A. 2000. Early stages of evolution of the Black Sea. Geological Society, London, Special Publications, 173(1), 235-249.

Küçük, H. M. 2016. Batı Karadeniz Zonguldak-Amasra açıklarında gaz ve gaz hidratların jeolojik ve jeofizik yöntemlerle araştırılması, Doktora Tezi. Dokuz Eylül Üniversitesi.

Kvenvolden, K. A. 1995. A review of the geochemistry of methane in natural gas hydrate. Organic Geochemistry, 23(11–12), 997–1008.

Lee, J. Y., Ryu, B. J., Yun, T. S., Lee, J., Cho, G. C. 2011. Review on the gas hydrate development and production as a new energy resource. KSCE Journal of Civil Engineering, 15(4), 689–696.

Lerche, I., Bagirov, E. 1998. Guide to gas hydrate stability in various geological settings. Marine and Petroleum Geology, 15 (1), 427-437.

Lericolais, G., Bourget, J., Popescu, I., Jermannaud, P., Mulder, T., Jorry, S., Panin, N. 2013. Late Quaternary deep-sea sedimentation in the western Black Sea: New insights from recent coring and seismic data in the deep basin. Global and Planetary Change, 103, 232–247.

Milkov, A., Sassen, R. 2000. Thickness of the gas hydrate stability zone, Gulf of Mexico continental slope. Marine and Petroleum Geology, 17(9), 981–991.

Minshull, T. A., Marín-Moreno, H., Betlem, P., Bialas, J., Bünz, S., Burwicz, E., Cameselle, A. L., Çifçi, G., Giustiniani, M., Hillman, J., Hölz, S., Hopper, J. R., Ion, G., León, R., Magalhães, V., Makovsky, Y., Mata, P., Max, M. D., Nielsen, T., Vázquez, J. 2020. Hydrate occurrence in Europe: A review of available evidence. Marine and Petroleum Geology, 111, 735–764.

Nasıf, A., Özel, E., Dondurur, D. 2020. Seismic identification of gas hydrates: a case study from Sakarya Canyon, western Black Sea. Turkish Journal of Earth Sciences, 29(3), 434-454.

Nikishin, A. M., Okay, A. I., Tüysüz, O., Demirer, A., Amelin, N., Petrov, E. 2015. The Black Sea basins structure and history: New model based on new deep penetration regional seismic data. Part 1: Basins structure and fill. Marine and Petroleum Geology, 59, 638–655.

Özel, Z., Dondurur, D., Klaucke, I. 2022. Seismic and geoacoustic evidence for subsurface fluid flow and seepage offshore Akçakoca, Southwestern Black Sea, Turkey. Geo-Marine Letters, 42(4).

Pape, T., Bahr, A., Klapp, S. A., Abegg, F., Bohrmann, G. 2011. High-intensity gas seepage causes rafting of shallow gas hydrates in the southeastern Black Sea. Earth and Planetary Science Letters, 307(1–2), 35–46.

Pape, T., Haeckel, M., Riedel, M., Kölling, M., Schmidt, M., Wallmann, K., Bohrmann, G. 2020. Formation pathways of light hydrocarbons in deep sediments of the Danube deep-sea fan, Western Black Sea. Marine and Petroleum Geology, 122, 104627.

Poort, J., Vassilev, A., Dimitrov, L. 2005. Did postglacial catastrophic flooding trigger massive changes in the Black Sea gas hydrate reservoir? Terra Nova, 17(2), 135–140.

Popescu, I., Lericolais, G., Panin, N., Wong, H., Droz, L. 2001. Late Quaternary channel avulsions on the Danube deep-sea fan, Black Sea. Marine Geology, 179(1–2), 25–37.

Popescu, I., De Batist, M., Lericolais, G., Nouzé, H., Poort, J., Panin, N., Versteeg, W., Gillet, H. 2006. Multiple bottom-simulating reflections in the Black Sea: Potential proxies of past climate conditions. Marine Geology, 227(3–4), 163–176.

Posewang, J., Mienert, J. 1999. The enigma of double BSRs: indicators for changes in the hydrate stability field? Geo-Marine Letters, 19(1–2), 157–163.

Reece, J. S., Flemings, P. B., Dugan, B., Long, H., Germaine, J. T. 2012. Permeability-porosity relationships of shallow mudstones in the Ursa Basin, northern deepwater Gulf of Mexico. Journal of Geophysical Research: Solid Earth, 117(B12), n/a-n/a.

Riedel, M., Bahk, J. J., Scholz, N., Ryu, B. J., Yoo, D. G., Kim, W., Kim, G. 2012. Mass-transport deposits and gas hydrate occurrences in the Ulleung Basin, East Sea – Part 2: Gas hydrate content and fracture-induced anisotropy. Marine and Petroleum Geology, 35(1), 75–90.

Robinson, A., Rudat, J., Banks, C., Wiles, R. 1996. Petroleum geology of the Black Sea. Marine and Petroleum Geology, 13(2), 195–223.

Römer, M., Sahling, H., Pape, T., Bahr, A., Feseker, T., Wintersteller, P., Bohrmann, G. 2012. Geological control and magnitude of methane ebullition from a high-flow seep area in the Black Sea—the Kerch seep area. Marine Geology, 319–322, 57–74.

Sloan, E. D., Koh, C. A. 2007. Clathrate Hydrates of Natural Gases. CRC Press.

Starostenko, V., Buryanov, V., Makarenko, I., Rusakov, O., Stephenson, R., Nikishin, A., Georgiev, G., Gerasimov, M., Dimitriu, R., Legostaeva, O., Pchelarov, V., Sava, C. 2004. Topography of the crust–mantle boundary beneath the Black Sea Basin. Tectonophysics, 381(1–4), 211–233.

Sun, Q., Alves, T. 2020. Petrophysics of fine-grained mass-transport deposits: A critical review. Journal of Asian Earth Sciences, 192, 104291.

Sun, Q., Alves, T. M., Lu, X., Chen, C., Xie, X. 2018. True Volumes of Slope Failure Estimated From a Quaternary Mass-Transport Deposit in the Northern South China Sea. Geophysical Research

Letters, 45(6), 2642–2651.

Thakur, N. K., Rajput, S. 2010. Exploration of Gas Hydrates. Springer Science and Business Media.

Tréhu, A., Long, P., Torres, M., Bohrmann, G., Rack, F., Collett, T., Goldberg, D., Milkov, A., Riedel, M., Schultheiss, P., Bangs, N., Barr, S., Borowski, W., Claypool, G., Delwiche, M., Dickens, G., Gracia, E., Guerin, G., Holland, M., Weinberger, J. 2004. Three-dimensional distribution of gas hydrate beneath southern Hydrate Ridge: constraints from ODP Leg 204. Earth and Planetary Science Letters, 222(3–4), 845–862.

Tugolesov, D. A., Gorshkov, A. S., Meysner, L. B., Soloviov, V. V., Khakhalev, E. M., Akilova, Yu. V., Akentieva, G. P., Gabidulina, T. I., Kolomeytseva, S. A., Kochneva, T. Yu., Pereturina, I. G., Plashihina, I. N. 1985. Tectonics of the Mesozoic Sediments of the Black Sea Basin. Moscow, Nedra [in Russian].

Vassiliev, A., Dimitrov, L. 2003. Model Evaluation of the Black Sea Gas Hydrates. Geophysique Ocenologie.

Winguth, C., Wong, H., Panin, N., Dinu, C., Georgescu, P., Ungureanu, G., Krugliakov, V., Podshuveit, V. 2000. Upper Quaternary water level history and sedimentation in the northwestern Black Sea. Marine Geology, 167(1–2), 127–146.

Wong, H. K., Winguth, C., Panin, N., Dinu, C., Wollschläger, M., Georgescu, P., Ungereanu, G., Krugliakov, V. V., Podshuveit, V. 1997. The Danube and Dniepr fans, morphostructure, and evolution. GeoEcoMarina, 2, 77–102.

Woodside, J. M., Ivanov, M. K. Limonov, A. F. 1997. Neotectonics and Fluid Flow Through Seafloor Sediments in the Eastern Mediterranean and Black Seas: Eastern Mediterranean Sea.

Yefremova, A. G., Zhizhchenko, B. P. 1974. Occurrence of crystal hydrates of gas in sediments of modern marine basins. Doklady Akademii Nauk SSSR, 214, 1179–1181.

Yoo, D. G., Kang, N. K., Yi, B. Y., Kim, G. Y., Ryu, B. J., Lee, K., Lee, G. H., Riedel, M. 2013. Occurrence and seismic characteristics of gas hydrate in the Ulleung Basin, East Sea. Marine and Petroleum Geology, 47, 236–247.

Zander, T., Haeckel, M., Berndt, C., Chi, W. C., Klaucke, I., Bialas, J., Klaeschen, D., Koch, S., Atgın, O. 2017. On the origin of multiple BSRs in the Danube deep-sea fan, Black Sea. Earth and Planetary Science Letters, 462, 15–25.

Zhang, X., Kong, G., Li, H., Wang, L., Yang, Q. 2022. Thermal conductivity of marine sediments influenced by porosity and temperature in the South China Sea. Ocean Engineering, 260, 111992.